

Active Sites Engineering toward Superior Carbon-Based Oxygen Reduction Catalysts via Confinement Pyrolysis

Sidi Wang, Qun He, Changda Wang, Hongliang Jiang,* Chuanqiang Wu, Shuangming Chen, Guobin Zhang, and Li Song*

Developing efficient and low-cost defective carbon-based catalysts for the oxygen reduction reaction (ORR) is essential to metal–air batteries and fuel cells. Active sites engineering toward these catalysts is highly desirable but challenging to realize boosted catalytic performance. Herein, a sandwich-like confinement route to achieve the controllable regulation of active sites for carbon-based catalysts is reported. In particular, three distinct catalysts including metal-free N-doped carbon (NC), single Co atoms dispersed NC (Co–N–C), and Co nanoparticles-contained Co–N–C (Co/Co–N–C) are controllably realized and clearly identified by synchrotron radiation-based X-ray spectroscopy. Electrochemical measurements suggest that the Co/Co–N–C catalyst delivers optimized ORR performance due to the rich Co–N_x active sites and their synergistic effect with metallic Co nanoparticles. This work provides deep insight for rationally designing efficient ORR catalyst based on active sites engineering.

Sluggish reaction kinetics of electrochemical oxygen reduction reaction (ORR) hinders the development of related energy storage and conversion techniques, especially metal–air batteries and fuel cells.^[1–4] To accelerate the reaction kinetics, developing efficient catalysts with well-designed structure characteristics is of great importance. Among these catalysts, defective carbon-based catalysts, typically transition metal and nitrogen codoped carbon (M–N–C) based materials, are extensively demonstrated as promising candidates due to earth-abundant and maneuverable properties.^[5–10] In these catalysts, investigation and identification of active sites have achieved considerable research and development attention due to its vital roles on the understanding of catalytic mechanisms. For the active sites of ORR, pyridinic and transition metal-coordinated N species are considered as the key to facilitate the ORR.^[11–17] Meanwhile, the transition metal nanoparticles also could boost the activities of the above active sites.^[18,19] Unfortunately, the defective carbon-based catalysts are usually obtained via a pyrolysis process of various

nitrogen and metal-containing precursors at high temperature, which does not allow much control over the form of these active sites.^[20,21] Therefore, developing novel synthesis methods for preparing catalysts with definite structures is highly desirable to overcome the obscuring from complex species and achieve precise evaluations for active sites.


In the synthesis of defective carbon-based catalysts, confinement pyrolysis is proved as an efficient method to prevent the aggregation of metal species under high-temperature pyrolysis processes, forming well-defined structures.^[22] Furthermore, to achieve the controllable regulation of active sites, the precursors for the formation of uniform and stable coating

layers in pyrolysis process are important to obtain stable active sites. Graphitic carbon nitride (g-C₃N₄), as one of typical carbon and nitrogen-containing materials, would undergo thermal decomposition under high temperature, thereby providing defective N-doped carbon layers and anchoring sites of metal species.^[23] Therefore, g-C₃N₄ would be a suitable platform to support the formation of specific structures, such as carbon-coating metal nanoparticles and defective carbon-anchored metal atoms.^[23,24] On the other hand, dopamine (DA), as one of nontoxic, sustainable, and N-containing biomolecules, is also used as a starting carbon precursor recently due to the readily spontaneous self-polymerization onto various substrates.^[25,26] This particular property endows it with potential to produce conformal coating on corresponding targets, thereby forming N-doped carbon coating layers and limiting the size of compounds under coating layers.^[6]

In this work, we developed a novel sandwich-like confinement pyrolysis route to synthesize defective carbon-based electrocatalysts for ORR, in which g-C₃N₄ and polydopamine (PDA) were used as inner sacrificial substrate and outer confinement layers, respectively. By tuning the dosages of Co source, three catalysts with different active sites, including metal-free N-doped carbon (NC), single Co atom dispersed NC (Co–N–C) and Co nanoparticles-contained Co–N–C (Co/Co–N–C), were elaborately constructed. The catalytic ORR performances of these materials were evaluated by systematic electrochemical measurements, establishing the correlation between structures and catalytic activities.

The main catalysts with three kinds of typical structure features were prepared with consecutive coating and pyrolysis

S. Wang, Q. He, C. Wang, Dr. H. Jiang, C. Wu, Dr. S. Chen, Prof. G. Zhang, Prof. L. Song
National Synchrotron Radiation Laboratory
CAS Center for Excellence in Nanoscience
University of Science and Technology of China
Hefei, Anhui 230026, P. R. China
E-mail: jhlworld@ustc.edu.cn; song2012@ustc.edu.cn

 The ORCID identification number(s) for the author(s) of this article can be found under <https://doi.org/10.1002/smll.201800128>.

DOI: 10.1002/smll.201800128

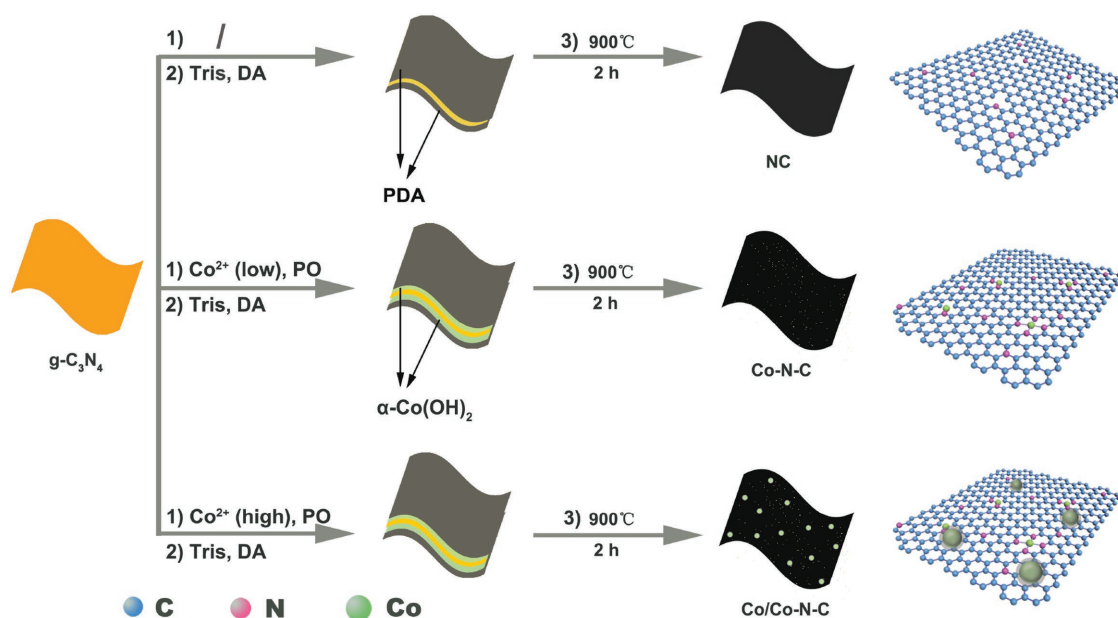


Figure 1. Schematic illustrations for the preparation of NC, Co–N–C, Co/Co–N–C, and corresponding structure models. Notes: 1) In situ preparation of α -Co(OH)₂ onto g-C₃N₄, 2) self-polymerization of DA under weakly alkaline solution, and 3) high-temperature pyrolysis under designed processes.

steps using g-C₃N₄ as the sacrificial substrate, as schematically illustrated in **Figure 1**. The g-C₃N₄ was synthesized by pyrolysis of urea at a high temperature of 550 °C (see more details in the Experimental Methods of the Supporting Information). The X-ray diffraction (XRD) and transmission electron microscopy (TEM) image indicate the characteristic interlayer stacking structure of aromatic systems with an interlayer spacing of 0.324 nm and a wrinkled sheet-like morphology (Figure S1, Supporting Information).^[27] Then, the propylene oxide-mediated alkalization method was used to in situ synthesize α -Co(OH)₂ coating layers onto the g-C₃N₄ substrate (marked as α -Co(OH)₂@g-C₃N₄, see more details in the Experimental Methods of the Supporting Information).^[28] The content of α -Co(OH)₂ was controlled by usage amount of salt precursor. Both α -Co(OH)₂ and g-C₃N₄ show corresponding diffraction peaks in XRD patterns, suggesting the successful preparation of α -Co(OH)₂@g-C₃N₄ compounds (Figure S2a, Supporting Information). No separate α -Co(OH)₂ nanosheets are observed in the TEM image, demonstrating the uniform α -Co(OH)₂ coating on the g-C₃N₄ substrate (Figure S2b, Supporting Information). This ideal coating effect is supposed to synthesize expected structures with conformal active species distribution. Subsequently, the PDA was used as the outer coating layers via the self-polymerization of DA under weakly alkaline condition (recorded as PDA@ α -Co(OH)₂@g-C₃N₄, see more details in the Experimental Methods of the Supporting Information). Negligible morphology change and no signs of free PDA suggest the perfect PDA coating (Figure S3, Supporting Information). As comparison, the PDA@g-C₃N₄ and PDA@ α -Co(OH)₂@GO (graphene oxide) were also prepared in similar conditions (Figures S4 and S5, Supporting Information).

These PDA-coating samples and α -Co(OH)₂@g-C₃N₄ were finally pyrolyzed under high temperature of 900 °C for 2 h (recorded as NC, Co/Co–N–C, Co–N–C, Co/NG, and Co/NC,

respectively, see more details in the Experimental Methods of the Supporting Information). The pyrolysis process resulted in the decomposition of g-C₃N₄ and PDA to form highly defective carbon layers with abundant N doping which readily reacts with Co and affords abundant Co, N-codoped carbon active sites.^[25,29] The detailed structures of the-obtained samples were first explored by XRD measurements. **Figure 2a** showed the XRD patterns of NC, Co–N–C, and Co/Co–N–C. As illustrated, the broad peak of metal-free NC from 23° to 28° reveals its typical defective structure probably due to the N-doping.^[30] As for Co–N–C, the only diffraction peak at 26.4° assigned to (002) plane of graphitic carbon can be observed. High angle annular dark field-scanning transmission electron microscopy was introduced to further investigate the detailed existence form of Co in Co–N–C. The bright points with atomic size confirm that Co is atomically dispersed without obvious aggregation (Figure S6, Supporting Information). However, the Co/Co–N–C shows graphitic C (002) peak and other two diffraction peaks at 44.2° and 51.5° which are consistent with the corresponding (111) and (200) planes of metallic Co nanoparticles. It is believed that the carbon graphitization can benefit the enhancement of the electronic conductivity and corrosion resistance of catalysts in electrocatalytic process.^[31] These results are also revealed by the corresponding TEM images (Figure 2b–d; Figure S7, Supporting Information). Obviously, the NC and Co–N–C show no signs of nanoparticles, while obvious nanoparticles can be observed in the Co/Co–N–C. In the PDA-free Co/NC and graphene-based Co/NG samples (see more details in the Experimental Methods of the Supporting Information), two metallic Co diffraction peaks are also displayed in the XRD patterns (Figure S8, Supporting Information). Notably, the Co/NC exhibits peaks of CoO, which probably stems from the surface oxidation of exposed Co nanoparticles due to the absence of PDA coating layers (Figure S8a, Supporting Information). It

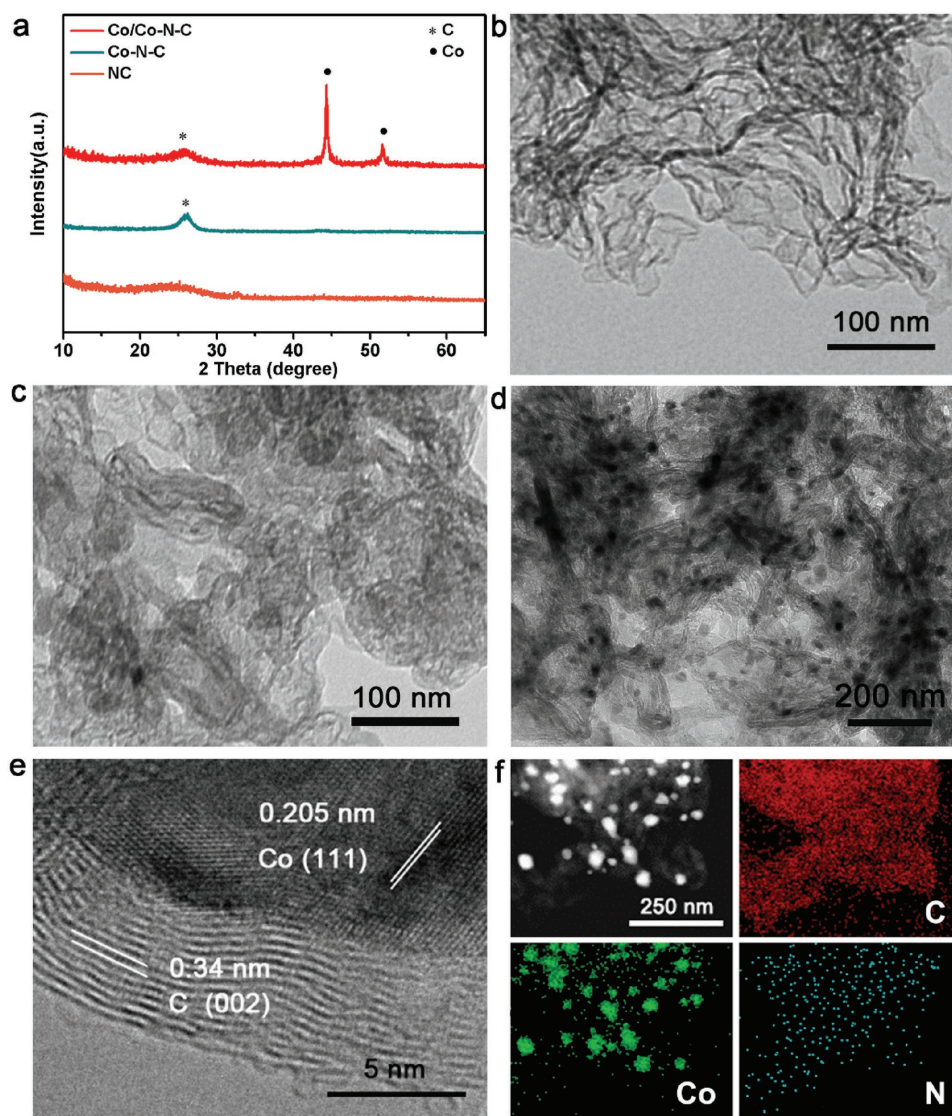


Figure 2. a) XRD patterns of the prepared NC, Co-N-C, Co/Co-N-C. Typical TEM images of b) NC, c) Co-N-C, and d) Co/Co-N-C. e) HRTEM image of the Co/Co-N-C sample. f) EDS elemental mapping for the Co/Co-N-C.

demonstrates the important role of PDA coating layers in inhibiting oxidation. The exposed nanoparticles are also revealed from TEM images (Figures S9 and S10, Supporting Information). Furthermore, the Co/NG sample shows sole and large Co nanoparticles without carbon coating layers (Figure S9, Supporting Information), which is significantly different from the homogeneously encapsulated Co nanoparticles with a small size of ≈ 25 nm in the Co/Co-N-C (Figure 2d). The obvious difference reveals the vital roles of $g\text{-C}_3\text{N}_4$ sacrificial substrate during pyrolysis process on reducing particle size and realizing complete carbon coating layers. Furthermore, the severe aggregation and large size of particles in Co/NC could be observed, which explains another positive role of PDA in preventing the aggregation and growth of the nanoparticles during the pyrolysis process. To realize close observation of the encapsulation structure, high-resolution TEM (HRTEM) measurement was also carried out. As can be seen in Figure 2e, the measured

plane spacing of 0.205 nm could be assigned to the (111) crystal plane of metallic Co, which was consistent with the aforementioned XRD result. Meanwhile, a ≈ 5 nm carbon layer with characteristic interlayer spacing of 0.34 nm uniformly coats onto Co nanoparticles. The elemental mapping for Co/Co-N-C was performed, as exhibited in Figure 2f. The high spatial correlation between C and N demonstrates that the carbon support is homogeneously doped with N inherited from PDA and $g\text{-C}_3\text{N}_4$ precursors. The individual and dramatic Co signal suggests the formation of dispersed Co nanoparticles. These results indicate that combining the merits of the C_3N_4 and PDA could promote the formation of highly defective N-doped carbon, and inhibit the growth of the metal nanoparticles to realize abundant Co-N species, which would be confirmed in the following section.

To determine the near-surface elemental compositions and the chemical states of the obtained samples, X-ray photoelectron spectroscopy (XPS) was applied. The XPS survey spectra

of Co/Co–N–C and Co/NG show the coexistence of C, N, O, Co elements (Figure S11, Supporting Information). The larger content of N in Co/Co–N–C reveals the positive role of the g-C₃N₄ precursor on providing N atoms. Besides, the presence of O in these composites could be attributed to the residual oxygen-containing species from these precursors and adsorbed oxygen on the surface.^[6] The C 1s spectrum of Co/Co–N–C was deconvoluted into several carbon bonding environments: 284.8 eV (C=C), 285.7 eV (C=N), 287.0 eV (C–N), and 291.3 eV (O–C=O), which suggests the successful doping of N atoms in the final carbon support layers (Figure S11b, Supporting Information). This N doping could be further evidenced by the fitted N 1s XPS spectrum. As shown in Figure S11c of the Supporting Information, three types of N species, namely, pyridinic or Co-coordinated N (398.7 eV), pyrrolic N (401.2 eV), and graphitic N (402.5 eV) suggest the existence of N-doped carbon support.^[32,33] In general, pyridinic and Co-coordinated N species are considered as active sites to achieve ORR.^[34–36] It is obvious that the overall fraction of pyridinic N in Co/Co–N–C is higher than that in Co/NG (Figure S12a, Supporting Information), while the ratio of pyrrolic N is low. This further verifies the positive role of g-C₃N₄ in improving active N species. To explore the formation of Co species, the Co 2p XPS spectrum was also fitted, as shown in Figure S11d of the Supporting Information. The Co 2p spectrum of Co/Co–N–C shows two pairs of main peaks corresponding to CoC_xN_y (780.5 and 795.3 eV), Co–N_x (782.6 and 797.8 eV), together with Co²⁺ shakeup satellite peaks (788.1 and 805.5 eV), verifying the formation of Co–N

bonds, one of the most active sites for the ORR.^[6] Notably, no XPS sign of metallic Co was detected, further confirming the whole encapsulation of Co nanoparticles into carbon coating layers. Furthermore, a similar fitting result of Co 2p in Co/NG was obtained, suggesting that the Co–N species are formed in carbon supports (Figure S12b, Supporting Information).

To deeply prove the structures of different samples, the X-ray absorption spectroscopy (XAS), one of the powerful tools to identify the coordination environment of center atoms, was carried out under the transmission mode.^[37] As shown in Figure 3a, the position of white line peak for Co/Co–N–C exists between those of Co foil and cobalt phthalocyanine (CoPc), indicating that the valence state of Co is situated between Co⁰ and Co²⁺. Meanwhile, the great similarity between Co/Co–N–C and Co foil demonstrates that the main state of Co was Co⁰, which is coincided well with the *k*²-weighted curves (Figure 3b).^[38] Similar result is also observed for Co/NG (Figure S13, Supporting Information) and consistent with the aforementioned XRD results. However, an obvious position difference of white line peak for Co–N–C is close to that of CoPc, suggesting the chemical state of main Co species in Co–N–C is Co²⁺ (Figure S14a, Supporting Information). This result is further confirmed by the corresponding *k*²-weighted curves (Figure S14b, Supporting Information), demonstrating the similar Co-related coordination environment between Co–N–C and CoPc with single Co atoms dispersion. The detailed structures of different samples are further corroborated with the Fourier transformed (FT) *k*²-weighted curves at the Co K-edge. In contrast to the Co foil and

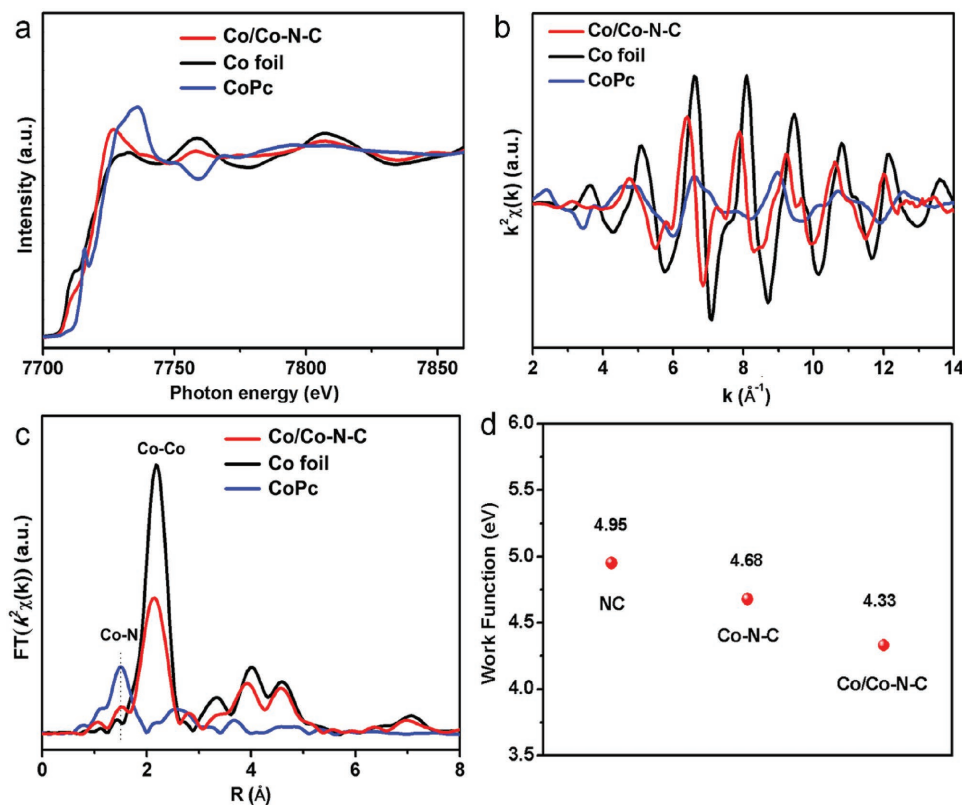


Figure 3. a) The normalized Co K-edge XANES spectra of Co/Co–N–C, Co foil, and CoPc. b) The XAFS spectra of Co/Co–N–C, Co foil, and CoPc in *k*-space and c) corresponding Fourier transformed XAFS spectra in *r*-space. d) Work functions for Co/Co–N–C, Co–N–C, and NC.

CoPc, the Co/Co–N–C presents a dominated peak at the position of $\approx 2.1 \text{ \AA}$ (Co–Co), suggesting the existence of metallic Co nanoparticles; meanwhile, a peak at $\approx 1.5 \text{ \AA}$ could be assigned to the Co–N bonds, supporting the simultaneous formation of Co–N_x species (Figure 3c).^[39] For the Co/NG, the lower back-scattering intensity than Co/Co–N–C is observed, indicating main presence of Co particles in Co/NG (Figure S15, Supporting Information). Notably, there were significant differences in atomic bonds between the FT k^2 -weighted curves for Co/Co–N–C and Co–N–C. The Co–N–C just exhibits one peak that can be only assigned to the Co–N bonds (Figure S16, Supporting Information). The above XAS analyses combining with aforementioned other spectroscopy and electron microscopy observations, we can identify three main samples with distinct structures: the high doping content N in NC, the single Co atoms in the Co–N–C without Co nanoparticles, and the Co nanoparticles in the Co/Co–N–C with abundant Co–N species.

As known, the work function (W_F) is the minimum energy for an electron to leave the surface of a material. Therefore, it would be one vital factor to evaluate the charge transfer process

in electrocatalysis. An ORR electrocatalyst with relatively low W_F could provide low energy barrier for donating electrons from the surface of the catalyst to the adsorbed oxygen, thus promote the generation of the OOH* species, which is considered to be the rate-determining path in the ORR.^[40,41] Here, the ultraviolet photoelectron spectroscopy test is carried out to explore the W_F difference for the obtained samples. The measured W_F values are 4.95, 4.68, and 4.33 eV for the NC, Co–N–C, and Co/Co–N–C, respectively. Compared to that of the Co–N–C, the lower W_F of the Co/Co–N–C is ascribed to the interfacial electrons transfer from the metal Co to the surrounding defective carbon layers.^[19] Considering of the lowest energy barrier, the Co/Co–N–C is expected easily to donate electrons from its surface to the adsorbed species, thus enabling the boosted catalytic reduction process.^[42]

To further confirm the proposed correlation between structure and catalytic properties, the ORR performances of the three samples were investigated in O₂-saturated 0.1 M KOH electrolyte. Figure 4a shows the well-defined cathodic peak for Co/Co–N–C in O₂-saturated electrolyte, indicating its

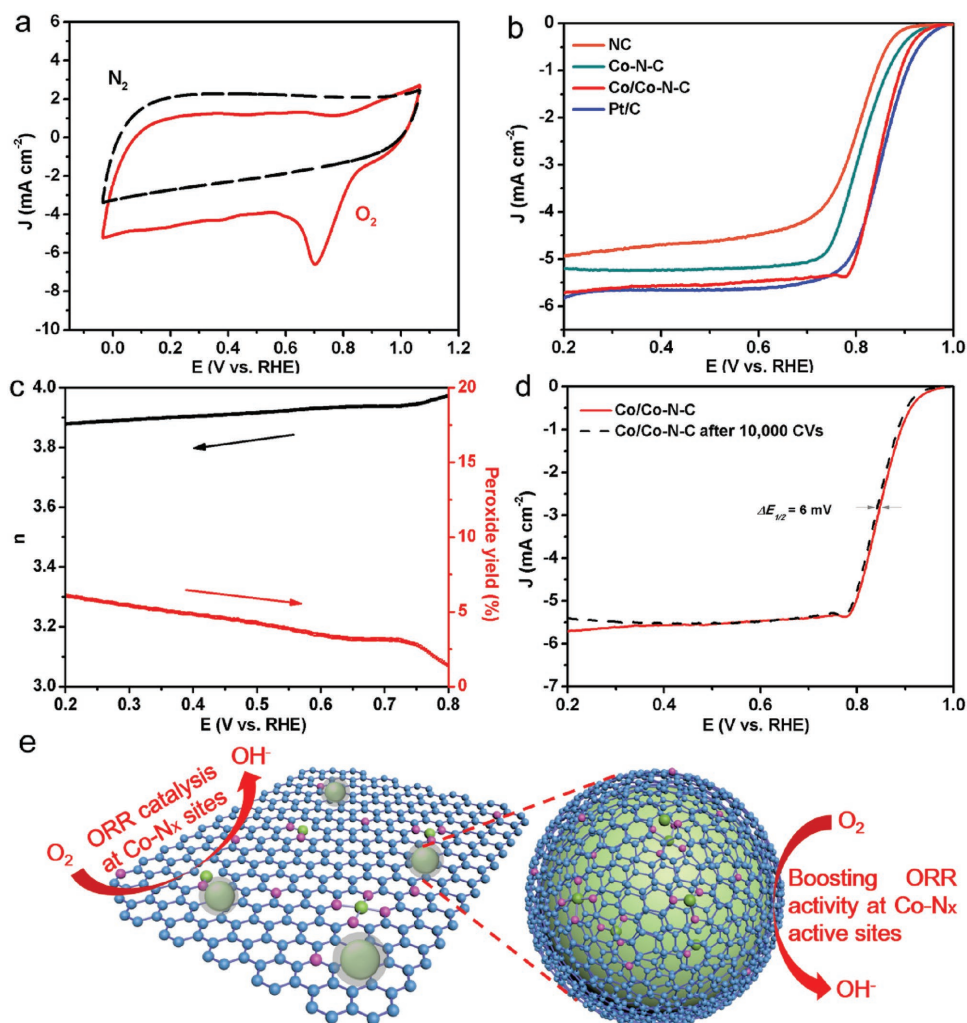


Figure 4. a) CV curves of Co/Co–N–C in N₂ and O₂-saturated 0.1 mol L⁻¹ KOH solution at a scan rate of 0.1 V s⁻¹. b) LSV curves of NC, Co–N–C, Co/Co–N–C, and Pt/C (20 wt%) at the rotation rate of 1600 rpm. c) Electron-transfer number (n) and peroxide yield (%) of Co/Co–N–C. d) LSV curves for Co/Co–N–C before and after 10 000 CV cycles. e) ORR scheme for Co/Co–N–C catalyst.

electrocatalytic activity toward ORR. In the linear sweep voltammetry (LSV) curves obtained from the rotating disk electrode experiments at the rotation rate of 1600 rpm, the Co/Co–N–C catalyst displays more positive onset ($E_{\text{onset}} = 0.97$ V vs reversible hydrogen electrode (RHE)) and half-wave potentials ($E_{1/2} = 0.85$ V vs RHE) than the NC (Figure 4b), which is probably attributed to the introduction of Co for forming Co-involved active sites. The LSV curves at different rotating speeds show the constant E_{onset} and increased current density (J) (Figure S17, Supporting Information). Moreover, upon introducing tiny Co dosage, the obtained Co–N–C also exhibits reduced ORR activity than the Co/Co–N–C, but is superior to the NC (Figure 4b). These results suggest that the Co nanoparticles existing in the defective carbon layers play the important role on boosting ORR performance. This conclusion could also be further proved by the significantly low ORR activity of Co/NG (Figure S18, Supporting Information) without the presence of carbon coating layers (Figure S9, Supporting Information). Besides the carbon coating layers, we also studied the role of metallic Co nanoparticles from another sight. After the acid treatment, the metallic Co nanoparticles in the Co/Co–N–C sample were mostly removed (Figure S19, Supporting Information), which can act as a control experiment for deep comparison. Subsequently, the LSV measurements suggest that the half-wave of the acid-treated Co/Co–N–C dropped to 0.823 V (vs RHE), strongly indicating the significance of metallic Co nanoparticles for enhanced ORR activity. Based on the above work function results, it is concluded that this existed Co nanoparticles could realize interfacial electron transfer from the Co to the surrounding Co–N_x species and thereby obtain the decreased activation energy of O₂ (Figure S20, Supporting Information).^[32,42,43] The Tafel slope of Co/Co–N–C (58.9 mV decade⁻¹) was apparently smaller than that of Co–N–C (73.3 mV decade⁻¹) and NC (68.9 mV decade⁻¹) (Figure S21, Supporting Information), which demonstrates the more favorable kinetics of Co/Co–N–C than Co–N–C and NC samples. This can be further confirmed by the mass activity (Figure S22, Supporting Information) and rotating ring-disk electrode measurements (Figures S23–S25, Supporting Information). Obviously, the higher mass activity (12.1 A g⁻¹) and near four-electron transfer numbers (>3.88) in potential region of 0.2–0.8 V (vs RHE) of the optimal Co/Co–N–C compared to that of Co–N–C and NC samples were achieved, further indicating the favorable kinetics of Co/Co–N–C (Figure 4c; Figures S26 and S27, Supporting Information). The electrochemical stability, another key factor for practical applications, was also studied. Strikingly, there was only 6 mV decline in $E_{1/2}$ even after 10 000 continuous CV cycling, clearly confirming that the Co/Co–N–C catalyst also exhibits excellent long-term durability superior to commercial Pt/C (Figure 4d; Figures S28 and S29, Supporting Information). The retained structure after durability test was also confirmed by careful TEM and HRTEM observations (Figure S30, Supporting Information). Furthermore, the ORR current density of Co/Co–N–C after 2 M methanol addition also remained very steady, suggesting its excellent methanol tolerance in alkaline solution (the inset in Figure S28, Supporting Information). Therefore, compared to the metal-free doped carbon and single Co atom dispersed NC catalysts, the Co nanoparticles-contained Co–N–C realized

through rational structure design displays much higher catalytic performance. The reason for the superior ORR performance in Co/Co–N–C can be illustrated in Figure 4e: the rich Co–N_x species in Co/Co–N–C act as active sites for ORR; meanwhile, the interfacial electrons transfer boosts the ORR activity of the Co–N_x sites around the Co nanoparticles.

In summary, we have successfully designed a sandwich-like confinement pyrolysis strategy for the controllable synthesis of defective carbon-based electrocatalysts for boosted ORR electrocatalysis. Meticulous characterizations have revealed that this strategy allowed efficient regulation over the active sites. The detailed electrochemical measurements have suggested that the Co/Co–N–C comprising metallic Co nanoparticles and defective carbon coating layers showed optimized performance for ORR with good selectivity (near four-electron process), stability, and tremendous immunity to methanol in alkaline medium. Considering these outstanding performance, it is believed that this work would open up new opportunities in designing efficient ORR catalysts for further development of metal–air batteries and fuel cells.

Supporting Information

Supporting Information is available from the Wiley Online Library or from the author.

Acknowledgements

S.W. and Q.H. contributed equally to this work. This work was financially supported by MOST (2017YFA0303500 and 2014CB848900), NSFC (U1532112, 11574280, 11605201, and 21706248), CAS Key Research Program of Frontier Sciences (QYZDB-SSW-SLH018), China Postdoctoral Science Foundation (BH2310000033), CAS Interdisciplinary Innovation Team, Innovative Program of Development Foundation of Hefei Center for Physical Science (T6FXCX003). L.S. acknowledges the recruitment program of global experts, the CAS Hundred Talent Program, Key Laboratory of Advanced Energy Materials Chemistry (Ministry of Education) Nankai University, Key Laboratory of the Ministry of Education for Advanced Catalysis Materials and Zhejiang Key Laboratory for Reactive Chemistry on Solid Surfaces (Zhejiang Normal University). The authors thank the Shanghai synchrotron Radiation Facility (14W1, SSRF), the Beijing Synchrotron Radiation Facility (1W1B and soft-X-ray Endstation, BSRF), the Hefei Synchrotron Radiation Facility (Photoemission, MCD and Catalysis/Surface Science Endstations, NSRL), and the USTC Center for Micro and Nanoscale Research and Fabrication for helps in characterizations.

Conflict of Interest

The authors declare no conflict of interest.

Keywords

active sites, confinement route, electrocatalysts, oxygen reduction reaction, X-ray absorption spectrum

Received: January 10, 2018

Revised: February 4, 2018

Published online:

- [1] L. Lin, Z. Yang, Y.-F. Jiang, A.-W. Xu, *ACS Catal.* **2016**, *6*, 4449.
- [2] Y.-C. Wang, Y.-J. Lai, L. Song, Z.-Y. Zhou, J.-G. Liu, Q. Wang, X.-D. Yang, C. Chen, W. Shi, Y.-P. Zheng, M. Rauf, S.-G. Sun, *Angew. Chem., Int. Ed.* **2015**, *54*, 9907.
- [3] Z. Pei, H. Li, Y. Huang, Q. Xue, Y. Huang, M. Zhu, Z. Wang, C. Zhi, *Energy Environ. Sci.* **2017**, *10*, 742.
- [4] Z. Zhang, M. Dou, H. Liu, L. Dai, F. Wang, *Small* **2016**, *12*, 1900.
- [5] W. Niu, L. Li, J. Liu, N. Wang, W. Li, Z. Tang, W. Zhou, S. Chen, *Small* **2016**, *12*, 1900.
- [6] S. H. Ahn, M. J. Klein, A. Manthiram, *Adv. Energy Mater.* **2017**, *7*, 1601979.
- [7] W. Jiang, L. Gu, L. Li, Y. Zhang, X. Zhang, L. Zhang, J. Wang, J. Hu, Z. Wei, L. Wan, *J. Am. Chem. Soc.* **2016**, *138*, 3570.
- [8] C. H. Choi, W. S. Choi, O. Kasian, A. K. Mechler, M. Sougrati, S. Brüller, K. Strickland, Q. Jia, S. Mukerjee, K. J. J. Mayrhofer, F. Jaouen, *Angew. Chem., Int. Ed.* **2017**, *56*, 8809.
- [9] G. Wu, K. L. More, C. M. Johnston, P. Zelenay, *Science* **2011**, *332*, 443.
- [10] Z. Zhang, M. Dou, H. Liu, L. Dai, F. Wang, *Small* **2016**, *12*, 4193.
- [11] D. Geng, N. Ding, T. A. Hor, Z. Liu, X. Sun, Y. Zong, *J. Mater. Chem. A* **2015**, *3*, 1795.
- [12] J. Li, Y. Zhang, X. Zhang, J. Han, Y. Wang, L. Gu, Z. Zhang, X. Wang, J. Jian, P. Xu, B. Song, *ACS Appl. Mater. Interfaces* **2015**, *7*, 19626.
- [13] K. A. Kurak, A. B. Anderson, *J. Phys. Chem. C* **2009**, *113*, 6730.
- [14] Y. J. Sa, D. J. Seo, J. Woo, J. T. Lim, J. Y. Cheon, S. Y. Yang, J. M. Lee, D. Kang, T. J. Shen, H. S. Shin, H. Y. Jeong, C. S. Kim, M. G. Kim, T.-Y. Kim, S. H. Joo, *J. Am. Chem. Soc.* **2016**, *138*, 15046.
- [15] Q. Lai, L. Zheng, Y. Liang, J. He, J. Zhao, J. Chen, *ACS Catal.* **2017**, *7*, 1655.
- [16] H. Wu, H. Li, X. Zhao, Q. Liu, J. Wang, J. Xiao, X. Guo, G. Wang, X. Bao, *Energy Environ. Sci.* **2016**, *9*, 3736.
- [17] X. Chen, F. Li, N. Zhang, L. An, D. Xia, *Phys. Chem. Chem. Phys.* **2013**, *15*, 19330.
- [18] W. Jiang, L. Gu, L. Li, Y. Zhang, X. Zhang, L. Zhang, J. Wang, J. Hu, Z. Wei, L. Wan, *J. Am. Chem. Soc.* **2016**, *138*, 3570.
- [19] D. Deng, L. Yu, X. Chen, G. Wang, L. Jin, X. Pan, J. Deng, G. Sun, X. Bao, *Angew. Chem., Int. Ed.* **2013**, *52*, 371.
- [20] S. Fu, C. Zhu, J. Song, D. Du, Y. Lin, *Adv. Energy Mater.* **2017**, *7*, 1700363.
- [21] L. Shang, H. Yu, X. Huang, T. Bian, R. Shi, Y. Zhao, G. I. Waterhouse, L. Wu, C. Tung, T. Zhang, *Adv. Mater.* **2016**, *28*, 1668.
- [22] Y. Wang, Y. Nie, W. Ding, S. Chen, K. Xiong, X. Qi, Y. Zhang, J. Wang, Z. Wei, *Chem. Commun.* **2015**, *51*, 8942.
- [23] H. Su, K. Zhang, B. Zhang, H. Wang, Q. Yu, X. Li, M. Antonietti, J. Chen, *J. Am. Chem. Soc.* **2017**, *139*, 811.
- [24] Y. Zheng, Y. Jiao, Y. Zhu, Q. Cai, A. Vasileff, L. Li, H. Han, Y. Chen, S. Qiao, *J. Am. Chem. Soc.* **2017**, *139*, 3336.
- [25] Y. Liu, F. Chen, W. Ye, M. Zeng, N. Han, F. Zhao, X. Wang, Y. Li, *Adv. Funct. Mater.* **2017**, *27*, 1606034.
- [26] H. Lee, S. M. Dellatore, W. M. Miller, P. B. Messersmith, *Science* **2007**, *318*, 426.
- [27] W. Gu, F. Lu, C. Wang, S. Kuga, L. Wu, Y. Huang, M. Wu, *ACS Appl. Mater. Interfaces* **2017**, *9*, 28674.
- [28] V. Oestreicher, M. Jobbagy, *Langmuir* **2013**, *29*, 12104.
- [29] C. Su, H. Cheng, W. Li, Z. Liu, N. Li, Z. Hou, F. Bai, H. Zhang, T. Ma, *Adv. Energy Mater.* **2017**, *7*, 1602420.
- [30] Q. Shi, Y. Wang, Z. Wang, Y. Lei, B. Wang, N. Wu, C. Han, S. Xie, Y. Gou, *Nano Res.* **2016**, *9*, 317.
- [31] L. Lin, Q. Zhu, A. W. Xu, *J. Am. Chem. Soc.* **2014**, *136*, 11027.
- [32] C. You, X. Jiang, L. Han, X. Wang, Q. Lin, Y. Hua, C. Wang, X. Liu, S. Liao, *J. Mater. Chem. A* **2017**, *5*, 1742.
- [33] S. Zhao, Y. Wang, J. Dong, C.-T. He, H. Yin, P. An, K. Zhao, X. Zhang, C. Gao, L. Zhang, J. Lv, J. Wang, J. Zhang, A. M. Khattak, N. A. Khan, Z. Wei, J. Zhang, S. Liu, H. Zhao, Z. Tang, *Nat. Energy* **2016**, *1*, 16184.
- [34] X. Ma, X. Zhao, J. Huang, L. Sun, Q. Li, X. Yang, *ACS Appl. Mater. Interfaces* **2017**, *9*, 21747.
- [35] W. Wu, Q. Zhang, X. Wang, C. Han, X. Shao, Y. Wang, J. Liu, Z. Li, X. Lu, M. Wu, *ACS Catal.* **2017**, *7*, 7267.
- [36] J. Wang, L. Li, X. Chen, Y. Lu, W. Yang, X. Duan, *Nano Res.* **2017**, *10*, 2508.
- [37] W. Liu, L. Zhang, W. Yan, X. Liu, X. Yang, S. Miao, W. Wang, A. Wang, T. Zhang, *Chem. Sci.* **2016**, *7*, 5758.
- [38] Y. Ye, H. Li, F. Cai, C. Yan, R. Si, S. Miao, Y. Li, G. Wang, X. Bao, *ACS Catal.* **2017**, *7*, 7638.
- [39] P. Yin, T. Yao, Y. Wu, L. Zheng, Y. Lin, W. Liu, H. Ju, J. Zhu, X. Hong, Z. Deng, G. Zhou, S. Wei, Y. Li, *Angew. Chem., Int. Ed.* **2016**, *55*, 10800; *Angew. Chem.* **2016**, *128*, 10958.
- [40] H. Yang, J. Miao, S. Hung, J. Chen, H. Tao, X. Wang, L. Zhang, R. Chen, J. Gao, H. Chen, L. Dai, B. Liu, *Sci. Adv.* **2016**, *2*, e1501122.
- [41] J. Y. Cheon, J. H. Kim, J. H. Kim, K. C. Goddeti, J. Y. Park, S. H. Joo, *J. Am. Chem. Soc.* **2014**, *136*, 8875.
- [42] J. Zhu, M. Xiao, Y. Zhang, Z. Jin, Z. Peng, C. Liu, S. Chen, J. Ge, W. Xing, *ACS Catal.* **2016**, *6*, 6335.
- [43] Y. Zhao, K. Watanabe, K. Hashimoto, *J. Am. Chem. Soc.* **2012**, *134*, 19528.